Local velocity measurements in heterogeneous and time-dependent flows of a micellar solution

J. P. Decruppe,[1,*] O. Greffier,[1] S. Manneville,[2] and S. Lerouge[3]
[1]*Laboratoire de Physique des Milieux Denses, 1 Bd. D. F. Arago IPEC CP87811 57078 Metz Cedex 3 France*
[2]*Centre de Recherche Paul Pascal, avenue Schweitzer 33000 Pessac, France*
[3]*Laboratoire Matière et Systèmes Complexes UMR 7057 Universitè Denis Diderot Paris VII, 2 place Jussieu Case 7056 75251 Paris Cedex 05*

(Received 27 January 2006; published 23 June 2006)

We present and discuss the results of pointwise velocity measurements performed on a viscoelastic micellar solution made of cetyltrimethylammonium bromide and sodium salicylate in water, respectively, at the concentrations of 50 and 100 mmol. The sample is contained in a Couette device and subjected to flow in the strain controlled mode. This particular solution shows shear banding and, in a narrow range of shear rates at the right end of the stress plateau, apparent shear thickening occurs. Time-dependent recordings of the shear stress in this range reveal that the flow has become unstable and that large sustained oscillations of the shear stress and of the first normal stresses difference emerge and grow in the flow. Local pointwise velocity measurements clearly reveal a velocity profile typical of shear banding when the imposed shear rate belongs to the plateau, but also important wall slip in the entire range of velocity gradients investigated. In the oscillations regime, the velocity is recorded as a function of time at a fixed point close to the rotor of the Couette device. The time-dependent velocity profile reveals random fluctuations but, from time to time, sharp decreases much larger than the standard deviation are observed. An attempt is made to correlate these strong variations with the stress oscillations and a correlation coefficient r is computed. However, the small value found for the coefficient r does not allow us to draw a final conclusion as concerns the correlation between stress oscillations and velocity fast decreases.

DOI: 10.1103/PhysRevE.73.061509 PACS number(s): 83.60.Wc, 83.50.Rp, 83.60.Rs

I. INTRODUCTION

Wormlike micellar solutions can be made in a very simple way by mixing a surfactant with a salt in water; in a wide range of concentration conditions, these simple systems show a great variety of rheophysical behaviors and have quite unusual mechanical as well as optical properties. In the dilute regime, for example, where the sample contains only a small amount of surfactant ($\simeq 0.1\%$ wt.), shear thickening is commonly observed [1–8]; the apparent viscosity increases sometimes by several orders of magnitude; shear induced structures (SIS) are assumed to be responsible for this phenomenon. A second domain of great physical interest is the semidilute regime, where one finds highly viscoelastic solutions containing long entangled micelles. Many solutions in this second region are accurately described by Maxwell's simple mechanical model in the linear range of strain or stress; but it is in the nonlinear regime that their most spectacular properties will be seen and shear banding certainly is one of these; numerous experimental work [9–14] have shown that the signature of shear banding is a flow curve made of three parts (see Fig. 1 for a schematic representation of the flow curve $\sigma(\dot{\gamma})$; a stress plateau AB separates two increasing branches OA' and B'C; the stress plateau is very similar to the plateau found in a first order phase transition: it is the locus of the stationary states of two phases with different rheophysical properties. Next to the moving wall grows the so-called induced phase supporting the highest shear rate $\dot{\gamma}_h$ and having the lowest viscosity η_h; it fills a proportion ϕ_h of the gap, the remaining part, $1-\phi_h=\phi_l$ corresponds to the less orientated layer subjected to $\dot{\gamma}_l$ and having the viscosity η_l.

Two very simple equations relates the rheological characteristics of the two phases:

(i) the lever rule that states that the macroscopic shear rate $\dot{\gamma}_M$ follows [15]:

$$\dot{\gamma}_M = \phi_l \dot{\gamma}_l + \phi_h \dot{\gamma}_h; \tag{1}$$

(ii) and the stress continuity at the interface between the two layers,

$$\frac{\eta_l}{\eta_h} = \frac{\dot{\gamma}_h}{\dot{\gamma}_l}. \tag{2}$$

The ratio of the viscosities is in the inverse ratio of the shear rates in the layers, and since $\dot{\gamma}_h > \dot{\gamma}_l$, the induced phase is less viscous than the primary one.

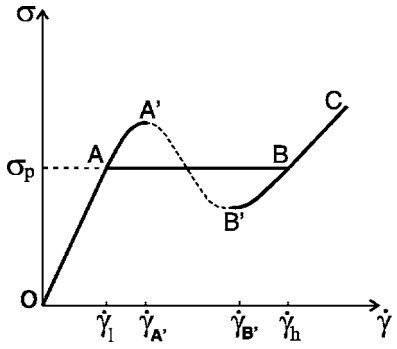

FIG. 1. Schematic representation of the nonmonotonic flow curve $\sigma(\dot{\gamma})$.

*Electronic address: Decruppe@univ-metz.fr

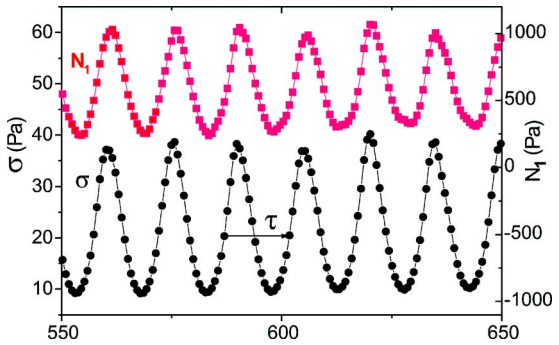

FIG. 2. (Color online) Oscillations of the shear stress σ and of the normal stress N_1 versus time a few minutes after the inception of the flow; σ (bottom curve with full black circles) and N_1 (top curve with full red squares). The macroscopic shear rate is $\dot{\gamma}_M = 5\ s^{-1}$ and τ is the period of the oscillations.

The right branch describes the state of the induced phase when the stress is increased. For most surfactant-salt systems, this branch is stable, at least in a restricted range of shear rates at the end of the plateau; this means that after a short period of time at the inception of the flow during which transient phenomena can be observed, the recorded stress or strain becomes time independent and the average values can be computed.

However, a few cases of unstable branches have been previously reported for different binary systems [16–19]. By unstable, one means that either the shear stress or the shear rate, depending on the operating mode, becomes time dependent, and undergo periodical variations. Other examples of oscillations and chaotic behavior have also been reported in various systems like lamellar and onion phases [20,21], and nematic liquid crystals [22]. Coupling between flow and SIS concentration [23] or between flow and microstructure [24] can destabilize the high shear rate branch and cause oscillations of the stresses: tangential σ and first normal stress difference N_1.

In a previous paper [19] we have described the rheophysical properties of the binary system CTAB/NaSal (50/100 mmol) that belongs to the semidilute regime; it is a nearly perfect Maxwellian fluid with a single relaxation time $\tau = 2.65 \pm 0.15$ s; shear banding occurs in a range of shear rates extending between 0.45 ± 0.05 to $4.75 \pm 0.25\ s^{-1}$. The high shear rate branch is unstable and both the shear stress σ and normal stress N_1 oscillate with a period of approximately 15 ± 0.2 s (see in Fig. 2, a few periods of $\sigma(t)$ and $N_1(t)$). These oscillations present a sharp shape asymmetry: while the bottom part looks like the smooth variations of a sinusoidal function, the crests form a serrated profile. During an oscillation, the stress relaxes and decreases to a minimum very close to the stress plateau $\sigma_p \simeq 10$ Pa. On the basis of these particular features of the stress σ, we express the hypothesis that slip at the moving wall may occur when the stress reaches the crest of an oscillation. In order to check this assumption, we have performed pointwise velocity measurements (PVM) with a technique called ultrasonic speckle velocimetry [25] and based on the cross-correlation between high frequency ultrasonic speckles backscattered by seeds flowing with the sample. In this paper we report on the rheological behavior and PVM performed on the above-mentioned micellar system. The velocity profiles are compared to the stress variations that are recorded simultaneously. Correlations between stress relaxation and velocity decrease are searched for in order to check the assumption of slip at the moving wall when the stress oscillates.

II. SAMPLE AND EXPERIMENTAL DEVICES

A. The micellar system: CTAB/NaSal 50/100 mmol

The surfactant, cetyltrimethylammonium bromide (CTAB) and the organic salt, sodium salicylate (NaSal), were, respectively, purchased from Acros Organics and Aldrich. Both chemicals are used without further purification. Weighted amount of surfactant and salt are dissolved in distilled water to prepare the 50/100 mmol sample. The fluid is subjected to ultra sonic waves for a few hours and finally kept at 30 °C at least for three days prior to any experiments. During an experiment, the temperature is kept constant at 23 ± 0.1 °C. Glass spheres (mean diameter $\simeq 10\ \mu$m) are added to the solution used for the PVM. In the following and in order to be more concise, this solution will be referred to as solution S_2; its rheological behavior will be compared to the same solution but free of seeds and called S_1.

B. The device for performing PVM and rheology

The sample is subjected to shear flow in a transparent Couette cell. The diameter of the inner rotating cylinder (rotor) is 47 mm while the fixed outer one (stator) has a diameter of 50 mm, thus giving a gap of 1.5 mm. The rheometer (TA Instruments AR 1000) monitoring the cell is operating in a strain controlled mode. The PVM measurements are performed simultaneously to the stress recording. The velocity measurements are fast and a full profile can be drawn in as little as 0.02 to 2 s depending on the shear rate; the device offers a spatial resolution of 40 μm; it allows for the fine determination of velocity profiles in complex fluids and thus is particularly interesting when flow instabilities like shear banding or stress oscillations occur. A full description of the technique is given with many details in Ref. [25].

III. RHEOLOGICAL PROPERTIES OF THE SYSTEM

A. Flow curve in stress and shear rate controlled modes

In order to enhance the contrast of the sample to ultrasonic waves, it has to be seeded with small particles (glass or polystyrene spheres at the concentration of 1% wt.); one may wonder whether micron-sized particles introduced in the sample will change its rheological properties in a significant way; this is the reason why we compare the flow curve of the same sample with and without seeds (see Fig. 3). The set of full black circles • and open blue triangles (△), respectively, represent the flow curve $\sigma(\dot{\gamma})$ of the samples S1 and S2 in the strain controlled mode. The open red circles represent the same curve in the stress controlled mode and it is just drawn for comparison. In the small insert, the flow curves are represented on an enlarged scale in the shear thickening region.

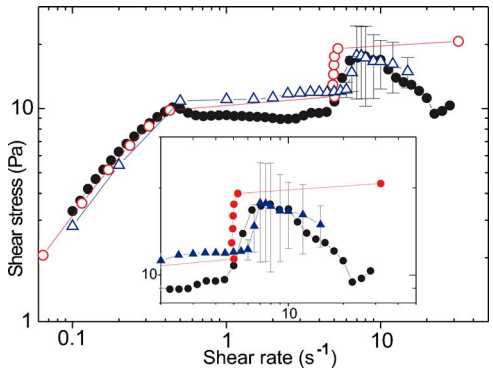

FIG. 3. (Color online) Flow curves $\sigma(\dot{\gamma})$ of the CTAB/NaSal 50/100 mmol solution in devices operating in strain and stress controlled modes; full black circles (•): $\sigma(\dot{\gamma})$ for the sample free of markers, open blue triangles (△): seeded solution; the open red circles (◦) is the flow curve in a stress controlled mode. The small inset is an enlargement of the shear thickening region where oscillations of the stress take place. The error bars represent the standard deviation of the shear stress.

As concerns the curve corresponding to solution S_2, the error bars give the order of magnitude of the oscillations that emerge and grow in the shear thickening region. The overall rheological behavior is very similar in both cases. One can observe a nearly linear branch in the low shear rates range, the stress plateau characteristic of shear banding and the upper branches which are the locii of the unstable states. The first branches end at the first critical shear rate $\dot{\gamma}_l$ and, for both solutions, the experimental value are very close: 0.45 ± 0.05 s^{-1} for solution S_1 and 0.5 s^{-1} for S_2; thus the addition of small spherical diffusers does not significantly change the behavior of the fluid in the first linear domain.

In the strain controlled mode and for solution S_2, the stress plateau presents a small positive slope; it is a consequence of the stress inhomogeneity due to the cylinders curvature of the Couette device. Experiments on solution S_1 were performed in a cone and plate device, where this disadvantage does not hold: the stress and the shear rate are homogeneous and constant throughout the gap. After the metastable region (see in Fig. 3 the flow curve with the full black circle •, the stress plateau decreases at first very gently to 8.9 Pa when $\dot{\gamma}_M$ reaches 3 s^{-1} before increasing again right to the end of the plateau. The small negative slope of the first part of the plateau may indicate that the steady state is not completely achieved when the stress is averaged by the device. The main difference is found in the shear rate ending the plateau (respectively, 4.75 ± 0.25 and 6 s^{-1} for the free and seeded sample). The seeded solution strongly scatters light, thus forbidding the use of flow birefringence to directly check for shear banding; however, the velocity profile described in the next section, will confirm that the small glass particles do not basically change the flow behavior.

B. Stress as a function of time when a constant shear rate is imposed

A sample of solution S_2 is subjected to an imposed shear rate and the stress σ is recorded as a function of time. Although the most interesting range of shear rates is the one covering the narrow shear thickening region, the temporal behavior of σ has also been studied in the first linear domain and on the stress plateau; the reason for these experiments is to make sure that the flow remains stationary outside the shear thickening domain. Figure 4 displays a few recordings of $\sigma(t)$ for three values of the shear rates: 0.2 (black circles ◦), 2 (red squares □), and 4 s^{-1} (blue triangles △). Apart from a short period of time corresponding to the transient regime, the shear stress is time independent in these two domains.

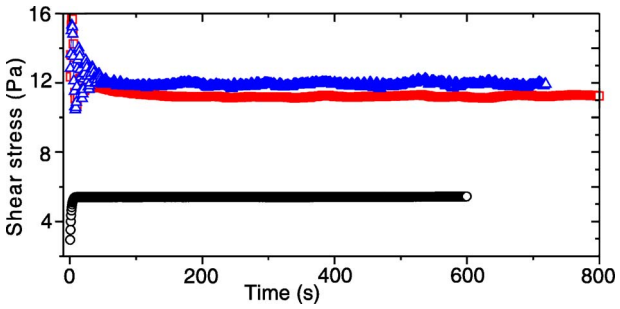

FIG. 4. (Color online) Time variations of the shear stress for three imposed shear rates $\dot{\gamma}_M$: in the linear domain, 0.2 s^{-1} black circles (◦), on the stress plateau: 2 s^{-1} (red squares □) and 4 s^{-1} (blue triangles △).

Figures 5(a) and 5(b) display the recorded signal when the imposed shear rate is chosen in the shear thickening region. After the inception of the shearing, the flow does not return to a steady state, but sustained oscillations emerge and grow. A spectral analysis (Fig. 5(c)) of $\sigma(t)$ reveals a broad peak with a maximum at a frequency $f_M=0.107$ Hz corresponding to a period of 9.34 s. Several secondary peaks close to the maximum appear in the expansion, they account for the long time range variations of σ; as a matter of fact, the end to end amplitude of the oscillations is not constant but is subjected to large variations on a time scale long compared to the period of the oscillations.

The main quantitative result is the value of the period of the signal that is only 9.34 s; this value is roughly 40% smaller than the period of the oscillations found in the solution free of seeds. This disagreement shows the importance of the experimental conditions in which measurements are performed; Fig. 2 displays results of earlier experiments done in a cone plate device while the PVM setup uses a Couette device.

In summary, when one compares the behavior of the sample with or without small glass spheres, it turns out that the rheology is qualitatively the same: a stress plateau corresponding to shear banding and time-dependent oscillations when the shear stress is chosen in the narrow shear thickening region at the end of the plateau.

IV. TIME AVERAGE VELOCITY PROFILES IN COUETTE FLOW

Local velocity profiles are measured by choosing the macroscopic shear rate in the same range as for the flow curve;

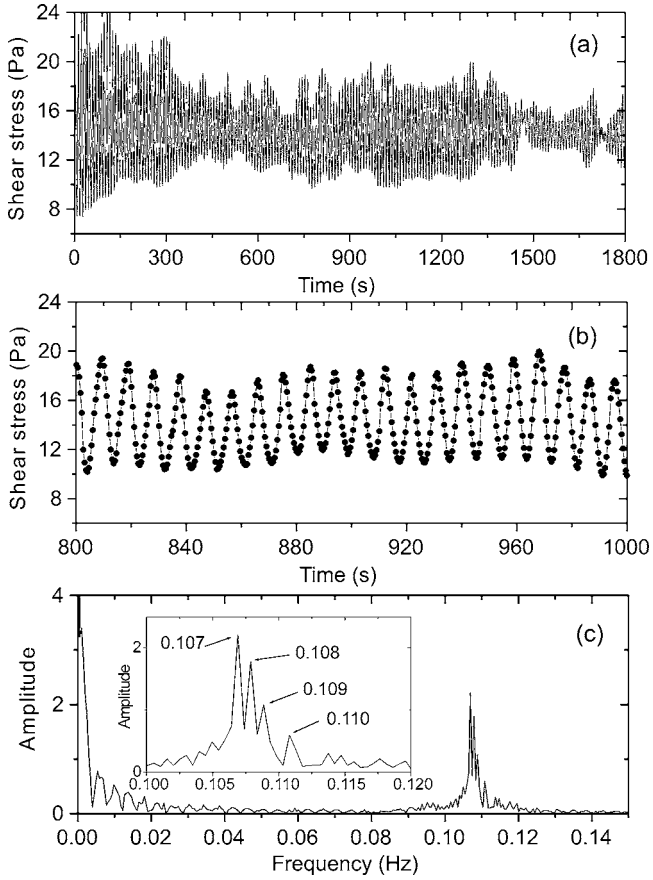

FIG. 5. Time variations of the shear stress σ (above) when the macroscopic shear rate is set to 7 s^{-1}. The bottom curve is the Fourier transform of the periodic signal, it has a broad peak with a maximum at 0.107 Hz (see the small inset for the detailed structure of the amplitude peak).

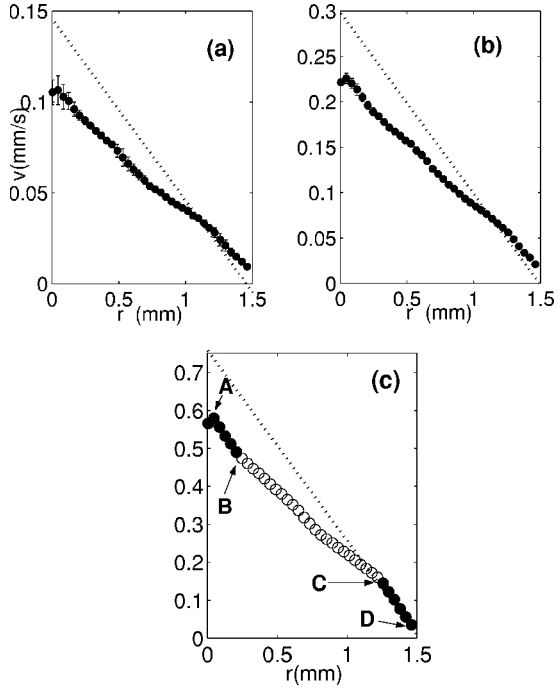

FIG. 6. Radial distribution of the average tangential velocity in the gap of a Couette cell. From left to right, the frames correspond to applied macroscopic shear rates $\dot{\gamma}_M$=0.1, 0.2, and 0.5 s^{-1}. The width of the gap is 1.5 mm; the dotted diagonal represents the ideal distribution for a Newtonian fluid. The profile at $\dot{\gamma}_M$=0.5 s^{-1} is made up of three segments AB (full black circle •), CD (full black circle •), and BC (open circle ◦).

we shall thus consider three zones: the low shear rate branch, the plateau region, and the narrow region, where shear thickening occurs, just after the plateau.

A. The low shear rate branch when $\dot{\gamma}_M < 0.5\ s^{-1}$

Figure 6 presents the distribution across the gap of the average tangential velocity when the macroscopic shear rate equals 0.1, 0.2, and 0.5 s^{-1}. Each curve is an average over several individual recordings of the velocity across the gap and the typical acquisition times τ_A for one profile in this range of shear rates appear in the last column of Table I. The errors bars represent the standard deviation of the velocity; fluctuations are particularly noticeable near the moving cylinder. The profile at 0.5 s^{-1}, for example, and that will deserve special analysis, is the result of averaging 12 velocity distributions across the gap.

Although the last value is the shear rate beginning the plateau, it is included in this first domain, since the velocity profile is very similar to the two others and no shear banding is observed. The left vertical side of a frame is the velocity axis and the value attached to the upper left corner corresponds to the velocity (mm/s) of the inner moving wall while the right lower one (r=1.5 mm) corresponds to 0. The dotted line joining the two opposite corners represents the expected profile for a Newtonian fluid. The important feature that one can immediately observe is that the velocity at both ends (r=0,1.5 mm) is different from the expected value: slip occurs at both walls: at r=0 the effective velocity v_e is different from the imposed tangential velocity v_M and at r=1.5 mm it is not zero. The same behavior is observed when $\dot{\gamma}_M$=0.2 and 0.5 s^{-1}.

Let the slip percentage at the rotor be defined by

$$\text{slip}\ \% = \frac{v_M - v_e}{v_M}. \tag{3}$$

The effective velocities of the fluid near the walls are found by performing a linear regression on the profile and finding the coordinates of the intersections of the straight line with the vertical axis. At the same time, the slope of the line

TABLE I. Macroscopic shear rates $\dot{\gamma}_M$, effective shear rates $\dot{\gamma}_{ef}$ computed from linear regressions performed on the tangential velocity profiles, slip %, and average acquisition time τ_A.

$\dot{\gamma}_M$ (s^{-1})	$\dot{\gamma}_{ef}$ (s^{-1})	slip%	$\tau_A(s)$
0.1	0.066	27	100
0.2	0.15	23	86
0.5	0.35	36[a]	20

[a]Linear regression performed on segment BC of Fig. 6(c).

TABLE II. Macroscopic shear rates $\dot{\gamma}_M$ and effective shear rates $\dot{\gamma}_{lef}$ and $\dot{\gamma}_{hef}$ in the shear induced bands. The fourth column contains the percentage of slip at the moving wall and the last, the acquisition time τ_A.

$\dot{\gamma}_M$ (s^{-1})	$\dot{\gamma}_{lef}$ (s^{-1})	$\dot{\gamma}_{hef}$ (s^{-1})	% slip	τ_A (s)
1	0.36	2.3	38	27
1.5	0.41	2.7	50	19
2	0.36	4.97	41	15
3	0.53	5.82	23	11
4	0.6	6.93	16	9
5	0.51	7.68	12	8
6	0.6	8.47	3	3

is the effective shear rate $\dot{\gamma}_{ef}$ in the fluid. Deviations from the expected values of the velocity as high as 30% are observed at the rotor while, near the stator, the liquid is not completely at rest but is still flowing with a very small velocity (0.01–0.02 mm/s).

The results of the fitting procedures and computations of the slip percentage are gathered in Table I.

One should not be too surprised to observe wall slip in the first linear part of the flow curve since it has already be seen in a lyotropic lamellar phase [26], in microgels [27], and even in a Newtonian fluid by Pit [28,29]. A good review of the phenomenon of wall slip in various fluids like polymer solutions, emulsions, and particle suspensions has been made by Barnes [30].

Special attention will be paid to the profile corresponding to $\dot{\gamma}_M = 0.5\ s^{-1}$ (see the curve in Fig. 6(c)). Contrary to the expected linear profile, the experimental points do not gather on a single straight line, but the profile appears as made up of three segments like AB (full black circle •), BC (open circle ◦) and CD (•); the outermost segments are parallel, have a nearly equal width ($\simeq$=240 μm) and a slope different from $\dot{\gamma}_M$ because of slip at the walls. The slope of segments AB and CD equals the 0.52 s^{-1} value very close to $\dot{\gamma}_M$. We do not know by now if this peculiar behavior has a physical origin or if it is just an artifact of the experimental device. One should, however, remember that 0.5 s^{-1} is just the beginning of the stress plateau that corresponds to the emergence of shear banding and, consequently, instabilities may arise in the flow for this peculiar shear rate.

B. The plateau region: $0.5 < \dot{\gamma}_M \leq 6\ s^{-1}$

With the seeded solution, the stress plateau extends between 0.5 and 6 s^{-1}; the velocity profiles have been recorded at macroscopic shear rates $\dot{\gamma}_M$ covering this whole range and the average acquisition time for each value of $\dot{\gamma}_M$ are gathered in the last column of Table II. It should be emphasized that these profiles are averages taken over several minutes ($\simeq$10nm) for each shear rate. In all cases, the flow was stationary. The small standard deviation of the velocity (nearly the size of the black full circles) confirms that the flow does not evolve significantly after several minutes.

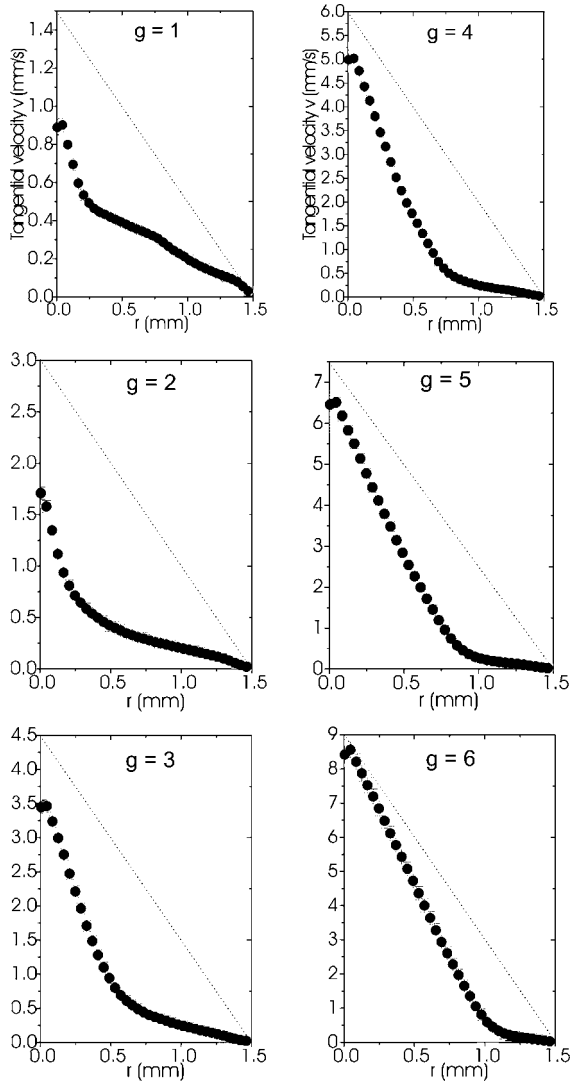

FIG. 7. Radial distribution of the average tangential velocity in the gap of a Couette cell. From left to right and top to bottom, the frames correspond to applied macroscopic shear rates chosen in the plateau range, the values of which appear in the frame. The width of the gap is 1.5 mm; the dotted diagonal represents the ideal Newtonian distribution.

Figure 7 displays these results for a few values of $\dot{\gamma}_M$ chosen between 1 and 6 s^{-1}. First of all one can easily notice that each curve consists of two segments having a different slope: this is the signature of shear banding; the flow is no longer homogeneous, but two layers supporting different velocity gradients coexist; one shall be called the l band and is subjected to the lowest rate $\dot{\gamma}_{lef}$ and the other one h band supporting $\dot{\gamma}_{hef}$. A second important feature observed in every graph is that slip still occurs at the moving wall; the fluid at the rotor is far from flowing with the imposed velocity and slip as high as 50% is observed at the beginning of the plateau for $\dot{\gamma}_M = 1.5\ s^{-1}$ (not shown in Fig. 7); on the contrary, near the stator, the fluid is nearly at rest, the effective velocity is very close to zero. An estimate of the local effective shear rates $\dot{\gamma}_{lef}$ and $\dot{\gamma}_{hef}$ in each band is merely deduced by performing linear regressions on the profiles. These results

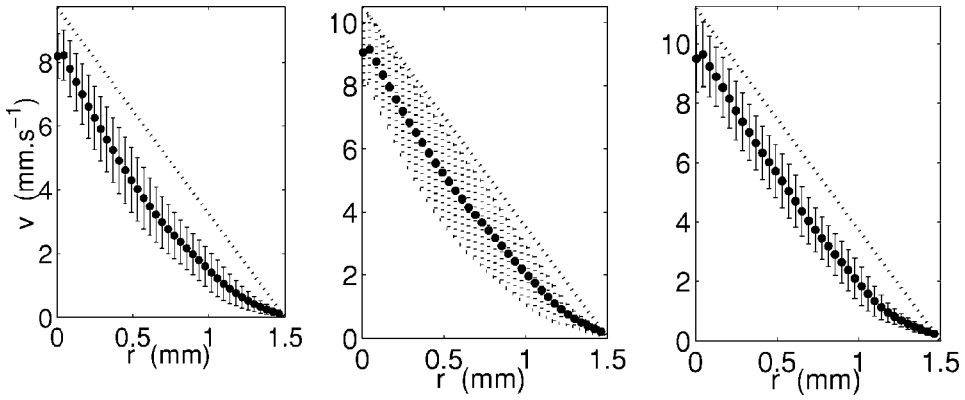

FIG. 8. Radial distribution of the average tangential velocity in the gap of a Couette cell. From left to right, the frames correspond to applied macroscopic shear rates $\dot{\gamma}_M$=6.5, 7, and 7.5 s^{-1}. The width of the gap is 1.5 mm; the dotted diagonal represents the ideal Newtonian distribution. The size of the error bars indicates that velocity fluctuations are important and that the flow is not stable anymore.

appear in Table II from which three general features come out.

(i) $\dot{\gamma}_{lef}$ is very close to $\dot{\gamma}_l$ (0.45±0.05 s^{-1}). As $\dot{\gamma}_M$ varies from 1 to 6 s^{-1}, the shear rate in the l band is not constant, but two domains where the values are rather close together can be distinguished; when the slip % is high, i.e., when $\dot{\gamma}_M$ belongs to $1 \leq \dot{\gamma}_M \leq 3$, approximately, $\dot{\gamma}_{lef}=0.37\pm0.03$ s^{-1}; on the other hand, when the slip % decreases, that is when $2.5 \leq \dot{\gamma}_M \leq 6$, $\dot{\gamma}_{lef}=0.54\pm0.06$ s^{-1}. This average value is the same as the one beginning the plateau in the flow curve (see Fig. 3).

(ii) $\dot{\gamma}_{hef}$ is not constant.

On the contrary, $\dot{\gamma}_{hef}$ is a monotonous increasing function of $\dot{\gamma}_M$; it reaches a maximum of 8.5 s^{-1} when $\dot{\gamma}_M$=6 s^{-1} with a slip % of only 3%. A macroscopic shear rate of 6 s^{-1} corresponds to the end of the stress plateau (see the flow curve in Fig. 3, but the velocity profile still shows two bands of unequal width, the one supporting the higher shear rate ($\dot{\gamma}_{hef}$) being the widest. Ignoring the small amount of slipping at the walls, one can probe the lever rule with $\dot{\gamma}_{hef}$=8.5 s^{-1} and $\dot{\gamma}_{lef}$=0.54 s^{-1}. A very simple computation [Eq. (1)] leads to $\dot{\gamma}_M \simeq 5.9$ s^{-1}, in excellent agreement with the imposed value. Thus, one comes to the important conclusion that $\dot{\gamma}_M$ =6 s^{-1} is not the real end of the plateau, as one could assume by looking at the flow curve; according to Spenley's theory [15], the plateau should end at $\dot{\gamma}_h$, i.e., at 8.5 and not 6 s^{-1}; the reason for this particular behavior is that the flow becomes unstable before the predicted 8.5 s^{-1} and temporal oscillations of σ and N_1 start to grow.

Once the critical shear rates are known and on the assumption that the stress is constant at the interface between the two layers, one can compute the ratio of the viscosity of both phases and get an estimate of the viscosity η_h of the induced phase,

$$\frac{\eta_l}{\eta_h} = \frac{\dot{\gamma}_{he}}{\dot{\gamma}_{le}} \simeq 16, \tag{4}$$

the viscosity η_l being calculated from the flow curve ($\eta_l \simeq 21$ Pa s), it turns out that $\eta_h \simeq 1.3$ Pa s. A rearrangement of the wormlike micelles in a highly orientated phase is usually put forward to explain this sharp decrease of the viscosity.

(iii) The slip percentage is not constant and apart from the experiment at 1.5 s^{-1} it decreases with the macroscopic shear rate $\dot{\gamma}_M$; another way to analyze this variation is to relate it to the proportion ϕ_h of the low viscosity induced phase that grows near the moving wall as $\dot{\gamma}_M$ goes over the stress plateau: the slip % is a linearly decreasing function of ϕ_h (not shown in the paper). In the flow of complex fluids, slip at a wall usually is explained by the emergence and the growth of a very thin lubricating layer between the wall and the fluid. Following Salmon *et al.* [26], one may write the thickness h of the layer as

$$h = \eta_s \frac{v_s}{\sigma}, \tag{5}$$

where η_s, v_s, and σ, respectively, the viscosity of the lubricating layer, the slip velocity [as defined in Eq. (3)] and the shear stress.

A quantitative estimate of the thickness h can now be made; in the worse condition (when the slip %=50%), the slip velocity $v_s \simeq 1.25$ mm/s and, for $\sigma=\sigma_p \simeq 10$ Pa, one gets a thickness $h \simeq 0.125\,\eta_s$ mm with η_s in Pa s.

If we assume that the lubricating layer is mainly made of water, we may expect that η_s will be of the same order of magnitude as the viscosity of water (10^{-3} Pa s). In that case, $h \simeq 0.125$ μm, a value that is far beyond the resolution of the measuring device ($\simeq$40 μm).

C. The narrow shear thickening region $6.5 < \dot{\gamma}_M < 7.5$ s^{-1}

Figure 8 displays three velocity profiles corresponding to shear rates chosen in the narrow shear thickening region at the end of the plateau. The two bands profiles observed in the previous range is replaced by a monotonous variation of the velocity in the gap. The slip at the moving wall still exists and the size of the error bars indicates that the flow undergoes very large fluctuations (especially important at $\dot{\gamma}_M$ =7 s^{-1}); the physical meaning of such a profile becomes questionable. The two band profile is replaced by a monotonous variation of the velocity in the gap; a single homogeneous band fills the gap.

V. CORRELATIONS BETWEEN TANGENTIAL VELOCITY AND SHEAR STRESS

In this section, we focus our attention on velocity measurements performed close to the moving wall in order to unveil a correlation between wall slip and the stress oscilla-

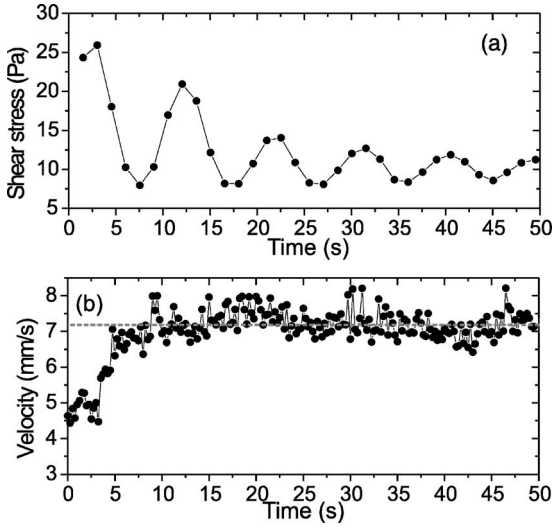

FIG. 9. Time variations of the shear stress σ (upper frame) and of the tangential velocity $v(t)$ (bottom curve) at the measurement point $r=0.15$ mm after the inception of the flow when the imposed shear rate is 5.5 s^{-1}. The horizontal straight dotted line drawn in the velocity frame indicates the mean velocity $\bar{v}=7.2$ mm/s with a standard deviation of 0.36 mm/s.

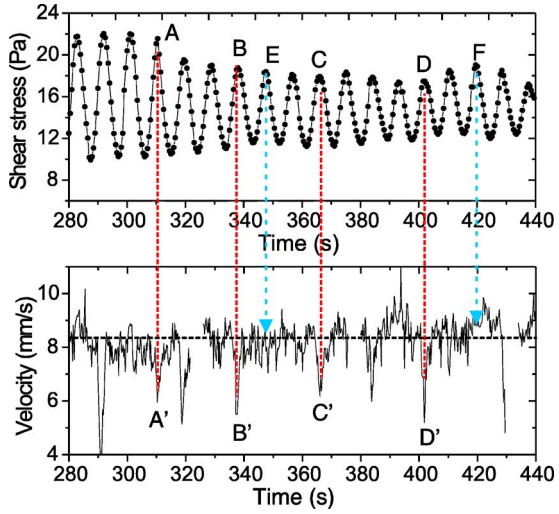

FIG. 10. (Color online) Time variations of the shear stress σ (upper frame) and of the tangential velocity $v(t)$ (bottom curve) after the inception of the flow when the imposed shear rate is 7 s^{-1} at the measurement point $r=0.15$ mm. The horizontal straight line drawn in the velocity frame indicates the mean velocity $\bar{v}=8.15$ mm/s. Capital letters mark a few particular points of both curves: dotted line (in red) like $AA'\ldots$ join a maxima of $\sigma(t)$ with a minima of $v(t)$ while dashed segments (in blue) link a peak of the stress with a point having approximately the mean velocity $\bar{v}$.

tions observed in the shear thickening region. By only recording a small part of the backscattered ultrasonic signal until the memory of the acquisition board is full, the temporal resolution is increased and velocities close to the rotor are accessed every 0.1 s at a typical shear rate of 7 s^{-1}. The drawback of this fast measurements mode is that some time is needed to transfer the data from the acquisition board to the computer memory before new data points can be recorded again. This leads to time gaps in the temporal velocity profiles, as can be seen in Fig. 10.

The velocity $v(t)$ that is plotted as a function of time is the result of an average over three measurement points at a distance $r=0.15$ mm from the rotor; the macroscopic shear stress is recorded simultaneously. We shall first investigate $v(t)$ and $\sigma(t)$ for a shear rate chosen on the plateau, i.e., $\dot{\gamma}_M=5.5$ s^{-1} and then the velocity gradient will be set to 7 s^{-1} in the shear thickening region.

A. $v(t)$ and $\sigma(t)$ when $\dot{\gamma}_M=5.5$ s^{-1}

In Sec. IV B, we have shown that the flow is heterogeneous and slip occurs at the moving wall: slip % $\simeq$9% when $\dot{\gamma}_M=5.5$ s^{-1}. Figures 9(a) and 9(b) display $\sigma(t)$ (top frame) and $v(t)$ (lower frame) during the first tens of seconds of the flow; at the inception of the flow, the stress undergoes an overshoot followed by damped oscillations before reaching again a steady state regime.

No clear correlations between $v(t)$ and $\sigma(t)$ are found: the velocity increases at first before fluctuating randomly around $(\bar{v})$. Identical observations (not shown in the paper) can be made further on when the stress has again found its steady value equal to σ_p.

B. $v(t)$ and $\sigma(t)$ in the shear thickening region

As previously mentioned, the crests of $\sigma(t)$ form a serrated profile with sharp peaks while the minima of the periodical signal follow smooth variations like a sinusoidal function; it seems that the stress is unable to reach its maximum value to form a rounded top before decreasing again; the slip at the moving wall is a possible explanation of this peculiar behavior, and thus it seems sensible to simultaneously record the temporal variations of the local velocity and of the shear stress.

Figure 10 displays the variations of the shear stress (upper frame) and of the velocity $v(t)$ (lower frame) after the inception of the flow and when the imposed shear rate is 7 s^{-1}. Capital letters are added to the graph in order to make the discussion easier: $A, B\ldots, A', B'\ldots$, respectively, refer to the maxima of the stress and minima of the velocity and dashed arrows (from E and F) link a maximum of σ with a point in the profile having a velocity close to the average velocity $\bar{v}$. The straight horizontal line in the $v(t)$ frame indicates the average velocity $\bar{v}$ (=8.15 mm/s).

Several general features can be drawn from the examination of Fig. 10.

(i) Despite the noise that can blur information, it seems that $v(t)$ undergoes periodical time variations.

(ii) Sharp peaks much larger than the standard deviation and corresponding to a fast decrease of the velocity are observed (points $A', B'\ldots$). Dotted lines are drawn to emphasize that, from time to time, a minimum of the velocity coincides with a maximum of the stress.

(iii) This is not true for all the maxima of the stress curve since a maximum of $\sigma(t)$ sometimes occurs when the velocity is approximately $\bar{v}$ (see the points at the end of the blue dashed arrows drawn from the points E and F).

(iv) The end to end amplitude of a stress oscillation is not directly correlated to the height of the corresponding velocity

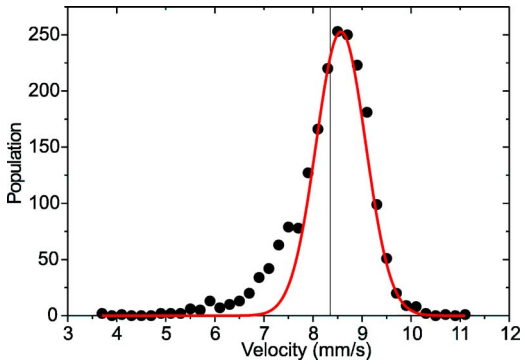

FIG. 11. (Color online) Distribution of velocity values as a function of the velocity near the moving wall over a period of time of 530 s. The counting interval is 0.2 mm/s in width. The vertical straight line is drawn at the abscissa of the mean velocity $\bar{v}$ =8.15 mm/s. The red curve represents the normal Gaussian distribution.

peak when it exists; compare, for example the relative amplitude of oscillations A, B, and D and the relative height of the peak A′, B′, and D′. One may expect a certain degree of correlation between the oscillation amplitude and the height of the velocity peak.

(v) The velocity values distribution is strongly asymmetrical (see Fig. 11). The vertical straight line marks the average velocity $\bar{v}$ and is drawn to emphasize that the distribution maximum is shifted to the right. The standard deviation is 0.8 mm/s; the distribution is quite narrow, most of the values are gathered around the maximum; however, the asymmetrical left tail shows that the distribution deviates from the normal distribution (see the red curve in Fig. 11 fitted with the experimental points on the right side of the vertical line) that we could expect if the fluctuations of the velocity were from a purely random origin.

(vi) Correlations between velocity and stress variations that shall validate or invalidate the wall slip hypothesis are searched for and a correlation coefficient r is computed from Eq. (6),

$$r = \frac{\Sigma(v_i - \bar{v})(\sigma_i - \bar{\sigma})}{[\Sigma(v_i - \bar{v})^2 \Sigma(\sigma_i - \bar{\sigma})^2]^{1/2}}; \tag{6}$$

$\bar{\sigma}$ and $\bar{v}$, respectively, stand for the average stress and tangential velocity; σ_i are the stress maximum and the v_i''s are the corresponding values of the velocity.

The correlation coefficient $r=-0.2$; the negative sign reveals that the maxima of the shear stress and the minima of the velocity vary in opposite direction. However, the relatively small value of $r^2=4\%$ does not allow for a final conclusion as concerns the correlation between stress and velocity.

One should also remember that the velocity profile is measured in a plane perpendicular to the vorticity at a particular height in the cell; there is no reason for the wall slip to happen all over the entire moving wall: the liquid could easily slip at some height in the cell without the recorded velocity showing a sudden decrease. This local change of the velocity would not be detected by the ultrasonic device, but would still influence the shear stress.

VI. CONCLUSION

In this paper, we have described and discussed experimental data representing the evolution of the shear stress and of the local tangential velocity in a viscoelastic micellar system made of CTAB and NaSal in water. The sample behaves like a good Maxwellian liquid with a single relaxation time and shear banding is expected to occur in some shear rates range. The experimental flow curve $\sigma(\dot{\gamma})$ in strain controlled mode is made of two branches separated by a stress plateau characteristic of heterogeneous flows in two layers. Pointwise velocity measurements have revealed that wall slip is present with more or less importance over the entire range of shear rates studied. However, it does not prevent the emergence of shear banding as confirmed by the velocity profiles measured in the plateau range. When the slip % is small (for shear rates near the right end of the stress plateau), one can make use of the lever rule to compute the critical shear rates at both ends of the plateau. If the lowest one, $\dot{\gamma}_l$ is in good agreement with the value beginning the plateau, it is not the same for $\dot{\gamma}_h$ that is supposed to end the plateau; the lever rule leads to 8.5 s^{-1} for $\dot{\gamma}_h$ when the flow curve only gives 6 s^{-1} for the right end of the plateau. This disagreement is easily understood when one knows that time periodic oscillations of the stress occur when the shear rate is slightly increased beyond $\dot{\gamma}_h$ (i.e., in the shear thickening region); thus the flow becomes unstable before the end of the plateau. We have put forward the hypothesis of wall slip to explain the asymmetrical shape of the stress oscillations, the crests of which look like a serrated profile. To check this assumption, velocity profiles as a function of time were recorded; they reveal that the mean velocity at $\dot{\gamma}_M=7$ s^{-1} is 22% lower than the expected value (10.5 mm/s); in addition to this average slip and apart from random fluctuations, $v(t)$ displays narrow descending peaks: the velocity decreases strongly in a very short time. From time to time, these peaks occur when the stress is at a maximum of an oscillation; it is then tempting to look for correlations between $\sigma(t)$ and $v(t)$. The correlation coefficient r is found negative, revealing that the stress and the velocity vary oppositely; however, its low numerical value does not allow for a final conclusion. Further velocity measurements appear to be necessary to get more information on wall slip and on its implication in the stress oscillations.

[1] H. Rehage and H. Hoffmann, Mol. Phys. **74**, 933 (1991).
[2] A. M. Wunderlich and P. O. Brunn, Colloid Polym. Sci. **267**, 627 (1989).
[3] J. F. Berret, S. Lerouge, and J. P. Decruppe, Langmuir **18**, 7279 (2002).
[4] Y. T. Hu, P. Boltenhagen, E. Matthys, and D. J. Pine, J. Rheol. **42**, 1209 (1998).
[5] V. Hartmann and R. Cressely, Colloid Polym. Sci. **276**, 169 (1998); Rheol. Acta **37**, 115 (1998).
[6] R. Gamez-Corrales and J. F. Berret, Langmuir **15**, 6755 (1999).
[7] R. Oda, P. Panizza, M. Schmutz, and F. Lequeux, Langmuir **13**, 6407 (1997).
[8] C. H. Liu and D. J. Pine, Phys. Rev. Lett. **77**, 2121 (1996).
[9] H. Rehage and H. Hoffmann, J. Phys. Chem. **92**, 4712 (1988).
[10] F. Pignon, A. Magnin, and J. M. Piau, J. Rheol. **40**, 573 (1996).
[11] J. F. Berret, G. Porte, and J. P. Decruppe, Phys. Rev. E **55**, 1668 (1997).
[12] S. Lerouge, J. P. Decruppe, and J. F. Berret, Langmuir **16**, 6464 (2000).
[13] J. P. Decruppe, R. Cressely, R. Makhloufi, and E. Cappelaere, Colloid Polym. Sci. **273**, 346 (1995).
[14] C. Grand, J. Arrault, and M. E. Cates, J. Phys. II **7**, 1071 (1997).
[15] N. A Spenley, M. E Cates, and T. C. B McLeish, Phys. Rev. Lett. **71**, 939 (1993).
[16] P. Fischer, Rheol. Acta **36**, 234 (2000).
[17] E. K. Wheeler, P. Fischer, and G. G. Fisher, J. Non-Newtonian Fluid Mech. **75**, 193 (1998).
[18] R. Bandyopadhyay, G. Basappa, and A. K. Sood, Phys. Rev. Lett. **9**, 2022 (2000).
[19] H. Azzouzi, J. P. Decruppe, S. Lerouge, and O. Greffier, Eur. Phys. J. E **17**, 507 (2005).
[20] J. B. Salmon, A. Colin, and D. Roux, Phys. Rev. E **66**, 031505 (2002).
[21] A. S. Wunenburger, A. Colin, J. Leng, A. Arneodo, and D. Roux, Phys. Rev. Lett. **86**, 1374 (2001).
[22] M. Grosso, S. Crescitelli, E. Somma, J. Vermant, P. Moldanaers, and P. L. Maffetone, Phys. Rev. Lett. **90**, 098304 (2003).
[23] V. Schmitt, F. Lequeux, A. Pousse, and D. Roux, Langmuir **10**, 955 (1994).
[24] S. M. Fielding and P. D. Olmsted, Phys. Rev. Lett. **92**, 084502 (2004).
[25] S. Maneville, L. Bécu, and A. Colin, Eur. Phys. J.: Appl. Phys. **28**, 361 (2004).
[26] J. B Salmon, S. Manneville, and A. Colin, Phys. Rev. E **68**, 051503 (2003).
[27] S. P. Meeker, R. T. Bonnecaze, and M. Cloitre, Phys. Rev. Lett. **92**, 198302 (2004).
[28] R. Pit, H. Hervet, and L. Léger, Phys. Rev. Lett. **85**, 980 (2000).
[29] C. Cottin-Bizonne, B. Cross, A. Steinberger, and E. Charlaix, Phys. Rev. Lett. **94**, 056102 (2005).
[30] H. A. Barnes, J. Non-Newtonian Fluid Mech. **56**, 221 (1995).